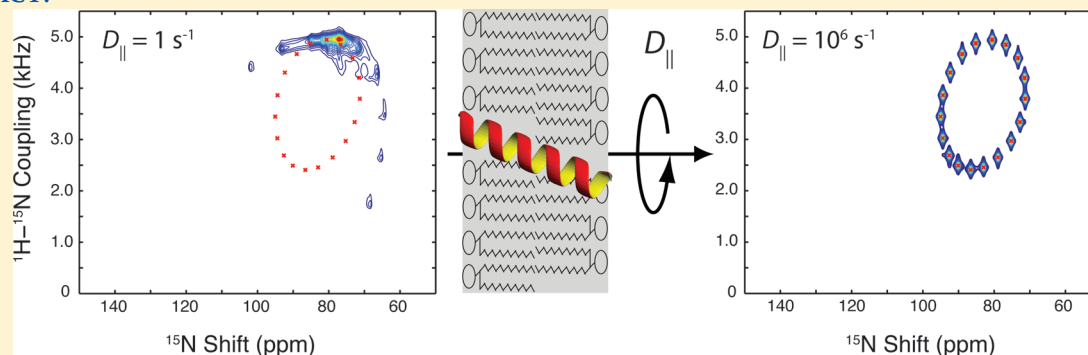


Orientational and Motional Narrowing of Solid-State NMR Lineshapes of Uniaxially Aligned Membrane Proteins

Alexander A. Nevzorov*

Department of Chemistry, North Carolina State University, 2620 Yarbrough Drive, Raleigh, North Carolina 27695-8240, United States

ABSTRACT:

A unified theory for the NMR line shapes of aligned membrane proteins arising from uniaxial disorder (mosaic spread) and global rotational diffusion about the director axis is presented. A superoperator formalism allows one to take into account the effects of continuous radiofrequency irradiation and frequency offsets in the presence of dynamics. A general method based on the Stochastic Liouville Equation makes it possible to bridge the static and dynamic limits in a single model. Simulations of solid-state NMR spectra are performed for a uniform α helix by considering orientational disorder and diffusion of the helix as a whole relative to the alignment axis. The motional narrowing of the resonance lines is highly inhomogeneous and can be used as an additional angular restraint in structure calculations. Experimental solid-state NMR spectra of Pf1 coat protein support the conclusions of the theory for two limiting cases. The static disorder dominates the ^{15}N NMR spectra of Pf1 aligned on a phage, while fast uniaxial diffusion provides a line narrowing mechanism for the Pf1 protein reconstituted in magnetically aligned bicelles.

1. INTRODUCTION

Magnetically aligned bicelles^{1–3} represent a useful mimetic for the structural studies of membrane proteins in their native-like, fully hydrated lipid environment. Structures of several membrane proteins reconstituted in bicelles have been obtained by solid-state NMR, the most notable examples being MerF,⁴ VPU,⁵ and Pf1.⁶ Moreover, sharp resonance lines have been recently obtained⁷ for the chemokine receptor CXCR1, which belongs to a class of G-protein coupled receptors (GPCRs) having seven transmembrane-spanning α helices. However, the natural aligned state for bicelles is that their membrane normals orient perpendicularly with respect to the main magnetic field. Even though parallel orientation can be achieved either by adding lanthanide ions⁸ or using biphenyl-containing lipids,⁹ perpendicular orientation often yields sharper resonances.¹⁰ This is due to the fact that the proton chemical shift dispersion is relatively narrow at this orientation; hence, the proton decoupling is more efficient, thus yielding narrower linewidths. In addition, at the perpendicular orientation, one obtains a more uniform magnetic alignment; consequently, the effect of mosaic spread (misalignment of the lipids and protein molecules) on the experimentally observed linewidths is less pronounced. It is important to note, however, that the benefits of the perpendicular orientation are essentially dependent upon the dynamic effects.

Fast (on the NMR time scale) small-amplitude fluctuations are usually manifested by the average order parameters, and a detailed study of these effects has been presented elsewhere.^{11–13} By contrast, the motional narrowing of NMR resonance lines is largely affected by the uniaxial rotational diffusion of a membrane protein as a whole within the bilayer.^{10,14,15} As for most, if not all, aligned samples, these effects are expected to be inhomogeneous due to the angular distributions of the orientations of the tensors for the relevant interactions (e.g., chemical shift anisotropy, CSA, or dipolar), which vary greatly throughout the protein backbone. Experimental and theoretical estimates of the correlation times for the uniaxial diffusion yield them on the microsecond time scale,^{14–19} that is, at or near the limit of the classical Redfield relaxation theory,^{20,21} which is generally applicable to fast motions. In addition, solid-state NMR experiments are usually performed under continuous radiofrequency (rf) irradiation of one or both channels, which modifies the relevant interaction Hamiltonians to achieve either heteronuclear decoupling or selective evolution of the dipolar couplings. Recently, a wealth of dynamic information contained in inhomogeneously broadened

Received: September 26, 2011

Revised: November 8, 2011

Published: November 10, 2011

The two main torsion angles are denoted as Φ_i and Ψ_i . The angle $\alpha_{\text{NC}_\alpha}$ is the angle between the N–C_α bond and the y -axis of the molecular frame (MF) corresponding to the i th peptide plane; γ_{tetra} is the tetrahedral angle; and $\gamma_{\text{C}_\alpha\text{C}'}$ is the angle between the C'–C_α bond and the y -axis of MF of the $(i+1)$ th plane. These angles are assumed constant and can be determined from the covalent peptide plane geometry:²⁹ $\alpha_{\text{NC}_\alpha} = 151.8^\circ$, $\gamma_{\text{tetra}} \approx 110.5^\circ$, and $\gamma_{\text{C}_\alpha\text{C}'} = 34.9^\circ$.

3. SUPEROPERATORS FOR SOLID-STATE NMR EXPERIMENTS

To calculate motional effects in the presence of rf irradiation, superoperator representation turns out to be very convenient, if not more rigorous. If the system of N spins of $1/2$ evolves under the (real) time-dependent Hamiltonian $H(t)$, its corresponding superoperator matrix $L(t)$ is given by³⁰

$$L(t) = H(t) \otimes \mathbf{1}_{2^N} - \mathbf{1}_{2^N} \otimes H^T(t) \quad (6)$$

Here where “ \otimes ” stands for the Kronecker product “ T ” stands for the matrix transpose, and $\mathbf{1}_{2^N}$ is a unit matrix of the size $2^N \times 2^N$. For the PISEMA-type experiments, the general form of the Hamiltonian is (in the units of rad s^{-1} , neglecting the proton CSA)

$$H(t) = \Delta\Omega I_z + \omega_S S_x + \omega_I I_x + \nu_{\text{CSA}} S_z + \nu_{\text{DIP}} I_z S_z \quad (7)$$

Here $\Delta\Omega$ is the proton frequency offset, and ω_S and ω_I are the amplitudes of the rf spin-lock fields for nitrogen and proton, respectively. The corresponding spin operators for the nitrogens and protons are denoted by $S_{x,z}$ and $I_{x,z}$ respectively. The time dependence is contained in the coefficients ν_{CSA} and ν_{DIP} when the azimuthal angle φ is stochastic. Only the nitrogen spin and its covalently bound amide proton are considered for simplicity. For the initial values of the density matrix

$$\rho(0) = S_x - I_x \quad (8)$$

its ensemble-averaged time evolution can be calculated as³⁰

$$\langle \text{vec } \rho(t) \rangle = \langle \exp_0 \{ i \int_0^t L(t') dt' \} \text{vec } \rho(0) \rangle \quad (9)$$

The symbol vec denotes the stacking operation of the columns of the density matrix.³¹ If the motions are sufficiently fast, the second-order cumulant expansion yields³⁰

$$\langle \text{vec } \rho(t) \rangle \approx \exp \{ it \langle L(t) \rangle - t \int_0^\infty d\tau \{ \langle L(\tau)L(0) \rangle - \langle L(\tau) \rangle \langle L(0) \rangle \} \} \text{vec } \rho(0) \quad (10)$$

Below we shall investigate the limits of applicability of eq 10 by comparing it with the more rigorous solution based on the Stochastic Liouville Equation,^{32–34} which takes into account the time correlations of all orders.

4. CLOSED FORM SOLUTIONS FOR CSA AND DIPOLAR RELAXATION

To obtain a closed-form solution in the perpendicular bicelles, eq 3 is explicitly evaluated for the case $\theta = \pi/2$ in the absence of

mosaic spread, $\Delta\theta = 0$. The final result is¹⁴

$$\nu_{\text{CSA}} = \frac{3}{2} \sigma_{\text{iso}} - \frac{\nu_{\text{CSA}}^{(0)}}{2} + \Delta\sigma (A_{\text{CSA}} \cos 2\varphi + B_{\text{CSA}} \sin 2\varphi) \quad (11)$$

where $\nu_{\text{CSA}}^{(0)}$ is given by eq 1 for the parallel orientation and the coefficients A_{CSA} and B_{CSA} are given by

$$A_{\text{CSA}} = \frac{3}{4} \sin^2 \beta_0 + \frac{\eta}{4} (1 + \cos^2 \beta_0) \cos 2(\alpha_0 - \gamma);$$

$$B_{\text{CSA}} = \frac{\eta}{2} \cos \beta_0 \sin 2(\alpha_0 - \gamma) \quad (12)$$

Similarly, for the dipolar couplings, one obtains

$$\nu_{\text{DIP}} = -\frac{\nu_{\text{DIP}}^{(0)}}{2} + \chi (A_{\text{DIP}} \cos 2\varphi + B_{\text{DIP}} \sin 2\varphi) \quad (13)$$

where $\nu_{\text{DIP}}^{(0)}$ is given by eq 2 and

$$A_{\text{DIP}} = \frac{3}{4} \sin^2 \beta_0 - \frac{3}{4} (1 + \cos^2 \beta_0) \cos 2\alpha_0;$$

$$B_{\text{DIP}} = -\frac{3}{2} \cos \beta_0 \sin 2\alpha_0 \quad (14)$$

For an arbitrary tilt angle θ , explicit evaluation of eq 3 is also straightforward, but the final expressions are more complicated and will not be given here.

Equation 10 allows one to obtain closed-form expressions for the transverse relaxation rates for the case of two spins. If one assumes complete heteronuclear decoupling, eq 10 can be evaluated in terms of the correlation functions corresponding to free rotational diffusion with the coefficient D_{\parallel} . By denoting

$$S_z = S_z \otimes \mathbf{1}_4 - \mathbf{1}_4 \otimes S_z \quad (15)$$

the decaying part of the CSA signal can be written as

$$\langle \text{vec } \rho(t) \rangle = \exp \{ -S_z^2 \Delta\sigma^2 t \int_0^\infty d\tau [A_{\text{CSA}}^2 \langle \cos 2\varphi(\tau) \cos 2\varphi(0) \rangle + B_{\text{CSA}}^2 \langle \sin 2\varphi(\tau) \sin 2\varphi(0) \rangle] \} \text{vec } \rho(0) \quad (16)$$

Noting that $S_z^2 \text{vec } \rho(0) = \text{vec } \rho(0)$ and calculating the correlation functions using the method outlined in ref 30 we get for the transverse relaxation rate and the full line width at half-height

$$R_2^{(\text{CSA})} = \pi \Delta \nu_{1/2}^{(\text{CSA})} = \frac{A_{\text{CSA}}^2 + B_{\text{CSA}}^2}{8D_{\parallel}} \Delta\sigma^2 \quad (17)$$

The case of the dipolar coupling is slightly more complicated. In the absence of the chemical shift evolution, one can use the truncated flip-flop Hamiltonian superoperator in the doubly tilted rotating frame,³⁰ viz.

$$C_{\pm} = \frac{(S_+ I_- + S_- I_+)}{4} \otimes \mathbf{1}_4 - \mathbf{1}_4 \otimes \frac{(S_+ I_- + S_- I_+)}{4} \quad (18)$$

It can be similarly shown that, for $\rho(0) = S_z - I_z$, $C_{\pm}^2 \text{vec } \rho(0) = 1/4 \text{vec } \rho(0)$, and the transverse relaxation rate and line width in the dipolar dimension become

$$R_2^{(\text{DIP})} = \pi \Delta \nu_{1/2}^{(\text{DIP})}$$

$$= \frac{A_{\text{DIP}}^2 + B_{\text{DIP}}^2}{32D_{\parallel}} \chi^2 = \frac{9\chi^2}{128D_{\parallel}} (1 - \sin^2 \beta_0 \cos^2 \alpha_0)^2 \quad (19)$$

Equations 17 and 19 show that the linebroadening due to uniaxial diffusion is expected to be highly inhomogeneous and contains the information about the orientation of the local director axis with respect to the local molecular frame as given by the angles α_0 and β_0 .

5. FORMULATION IN TERMS OF THE STOCHASTIC LIOUVILLE EQUATION

The ensemble-averaged exponential superoperator of eq 9 can be more rigorously evaluated by using the Stochastic Liouville Equation (SLE)^{32–34} that contains the mixing of the quantum spin space and the motional terms. Briefly, the SLE describes the time evolution of the generalized density state vector, $\mathbf{g}(\varphi, t)$

$$\frac{\partial \mathbf{g}(\varphi, t)}{\partial t} = (i\mathbf{L} + \Gamma)\mathbf{g}(\varphi, t) \quad (20)$$

where the diffusion operator is given by

$$\Gamma = D_{\parallel} \frac{\partial^2}{\partial \varphi^2} \quad (21)$$

To solve the SLE by standard methods of matrix algebra, we perform separation of variables and use the following expansion in the basis of sines and cosines¹⁴

$$\mathbf{g}(\varphi, t) = \sum_{n=0}^{N_{\max}-1} \mathbf{g}_n^c(t) \cos n\varphi + \sum_{n=1}^{N_{\max}} \mathbf{g}_n^s(t) \sin n\varphi \quad (22)$$

Usually $N_{\max} = 20$ is sufficient, and only the even coefficients n need to be considered for the case of perpendicular orientation. This yields a matrix representation for the part of the Liouvillian supermatrix corresponding to the CSA interaction in the Hilbert space

$$\mathbf{L}_{\text{CSA}} = \mathbf{S}_z \otimes \left[\left(\frac{3}{2} \sigma_{\text{iso}} - \frac{\nu_{\text{CSA}}^{(0)}}{2} \right) \mathbf{I}_{2N_{\max}} + \Delta\sigma(A_{\text{CSA}}\mathbf{M}_{\text{cos}} + B_{\text{CSA}}\mathbf{M}_{\text{sin}}) \right] \quad (23)$$

The matrices of the coupling coefficients \mathbf{M}_{cos} and \mathbf{M}_{sin} and for the diffusion operator Γ can be readily evaluated in terms of the normalized overlap integrals of the sine and cosine functions and have been given elsewhere.¹⁴ The part of the Liouvillian corresponding to the dipolar coupling is similarly given by

$$\mathbf{L}_{\text{DIP}} = \mathbf{C}_2 \otimes \left[\left(-\frac{\nu_{\text{DIP}}^{(0)}}{2} \right) \mathbf{I}_{2N_{\max}} + \chi(A_{\text{DIP}}\mathbf{M}_{\text{cos}} + B_{\text{DIP}}\mathbf{M}_{\text{sin}}) \right] \quad (24)$$

where the two-spin dipolar interaction superoperator matrix is given by

$$\mathbf{C}_2 = \mathbf{S}_z \mathbf{I}_z \otimes \mathbf{I}_4 - \mathbf{I}_4 \otimes \mathbf{S}_z \mathbf{I}_z \quad (25)$$

Generalizing the one-dimensional solution,¹⁴ one can express the two-dimensional time-domain NMR signal as a quadratic form

$$G(t_1, t_2) = \mathbf{g}_1^T \exp[(i\mathbf{L}_2 + \Gamma)t_2] \exp[(i\mathbf{L}_1 + \Gamma)t_1] \mathbf{g}_0 \quad (26)$$

Here $\mathbf{g}_1 = \text{vec } S_{xy} \otimes (1, 0, \dots, 0)^T$ is the detection vector, and $\mathbf{g}_0 = \text{vec } \rho(0) \otimes (1, 0, \dots, 0)^T$ is the starting vector corresponding to the uniform initial probability density in φ , both vectors having the total length $16 \times 2N_{\max}$. The superoperators corresponding to

the rf irradiation and constant frequency offsets can be similarly constructed. The Liouvillian for the first (indirect dimension), \mathbf{L}_1 , corresponds to the Hamiltonian given by eq 7, and the total exponential superoperator can be split into two parts as given by the frequency-switched Lee–Goldburg scheme³⁵ with $\Delta\Omega = \pm\omega_1/\sqrt{2}$ and $\pm\omega_s = \pm(3/2)^{1/2}\omega_1$. For the direct dimension (during the detection period), \mathbf{L}_2 is also given by eq 7, albeit with $\Delta\Omega = \omega_s = 0$. To speed up the calculations, the Liouvillian supermatrices are explicitly diagonalized using Matlab (Mathworks, Inc.). The spectrum is easily obtained from eq 26 by a two-dimensional Fourier transform.

The relation of the diffusion coefficient to the protein size can be estimated using the Saffmann–Delbrück equation. Approximating a membrane protein as a cylinder of radius R and height h , D_{\parallel} is estimated as³⁶

$$D_{\parallel} = \frac{kT}{4\pi R^2 h \eta} \quad (27)$$

For instance, for a small (i.e., single-helical) protein, $R \approx 10 \text{ \AA}$, $h \approx 40 \text{ \AA}$, and $\eta = 0.1 \text{ Pa} \cdot \text{s}$, we obtain: $D_{\parallel} = 8 \times 10^5 \text{ s}^{-1}$. For larger multihelical proteins, such as GPCRs, $R \approx 20 \text{ \AA}$ ^{37,38} and $D_{\parallel} = 2 \times 10^5 \text{ s}^{-1}$. If a membrane protein oligomerizes, this further reduces the diffusion coefficient. These simple estimates provide the range of values used in the theoretical simulations.

6. SIMULATIONS OF THE TWO-DIMENSIONAL PISEMA EXPERIMENT IN THE PRESENCE OF MOSAIC SPREAD AND UNIAXIAL DIFFUSION

Monte Carlo simulations of static uniaxial disorder²⁷ for the parallel and perpendicular orientations of an 18-residue α -helix (having the uniform values $\Phi = -65^\circ$, $\Psi = -40^\circ$) tilted at 20° relative to the membrane normal are shown in Figure 2. A Gaussian distribution function $\exp(-\ln 2 \Delta\theta^2 / \sigma_\theta^2) \sin \Delta\theta$ has been used for $\Delta\theta$ with $\sigma_\theta = \pm 0.5^\circ$ mosaic spread, and the angles ψ and φ have been uniformly distributed between 0 and 2π . It can be seen that even at such a relatively small mosaic spread the lines are broadened quite inhomogeneously, being narrower at larger CSA values and noticeably wider in the lower right portion of the spectrum; the same trend was observed in ref 39. If the membrane is tilted at 90° relative to the main magnetic field, the lineshapes follow a static cylindrical powder pattern, and the individual peaks can no longer be resolved. The inset shows the spectrum corresponding to an ultraslow motional limit obtained by solving the SLE for PISEMA, eq 26, with $D_{\parallel} = 1 \text{ s}^{-1}$. As can be seen from comparing the two spectra for the perpendicular orientation, this diffusion rate essentially corresponds to the static limit.

Figure 3 shows the effect of uniaxial motional narrowing on the averaging of the static mosaic spread for the parallel orientation ($\theta = 0$). The spectrum in Figure 3A was simulated with a $\pm 2^\circ$ mosaic spread using 10 000 Monte Carlo steps for the static angles $\Delta\theta$ and φ . The spectrum in Figure 3B was simulated by solving the SLE for the stochastic angle φ and $D_{\parallel} = 10^4 \text{ s}^{-1}$ at each of the 1000 Monte Carlo steps, yielding the random values for the tilt angle $\Delta\theta$. The spectrum in Figure 3C was simulated by averaging eq 3 over the angle φ with the same ($\sigma_\theta = \pm 2^\circ$) mosaic spread in the limit of ultrafast diffusion. As can be seen, the inhomogeneous line broadening of Figure 3A caused by the static mosaic spread becomes more homogeneous in the presence of uniaxial diffusion (cf. Figure 3B), and the lines become almost uniform in the limit of ultrafast diffusion rates (cf. Figure 3C).

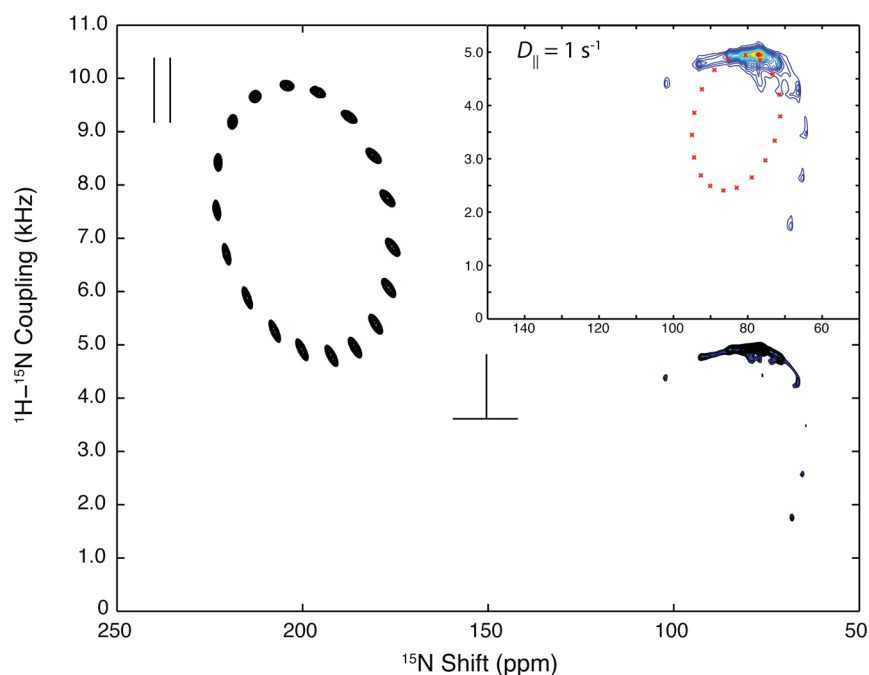


Figure 2. Static simulations of ^{15}N NMR spectra for a uniform α -helix ($\Phi = -65^\circ$, $\Psi = -40^\circ$) tilted at 20° relative to the membrane normal (local director axis). Simulations for the $\sigma_\theta = \pm 0.5^\circ$ mosaic spread are shown for the parallel and perpendicular orientations as indicated. Marked inhomogeneity in the linewidths is observed even when a small mosaic spread is present in the parallel orientation, whereas there are no resolved resonances in the perpendicular orientation due to the static uniaxial distribution about the director axis as given by the angle φ . Inset shows SLE simulations in the ultraslow motional limit with $D_{||} = 1 \text{ s}^{-1}$ for comparison. Red crosses show the calculated peak positions in the limit of fast uniaxial diffusion.

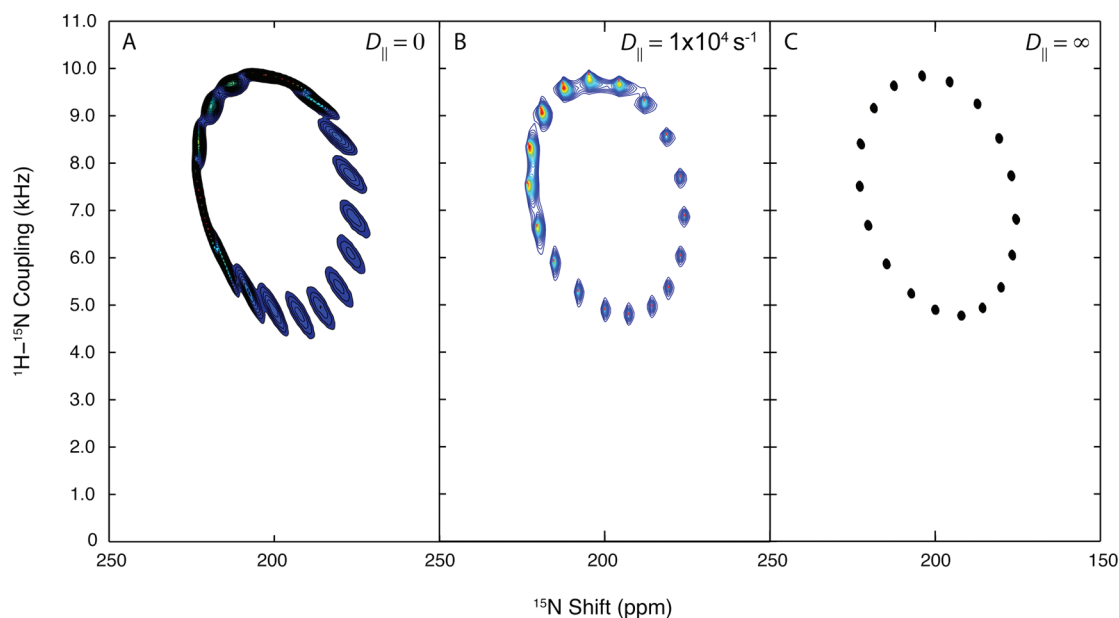


Figure 3. Effect of uniaxial diffusion on inhomogeneously broadened linewidths due to mosaic spread for the case of parallel alignment. (A) Static simulations for the $\pm 2^\circ$ mosaic spread in the angle θ and static uniaxial distribution in the angle φ . (B) SLE simulation of the $\pm 2^\circ$ mosaic spread in θ in the presence of uniaxial diffusion in the angle φ with $D_{||} = 10^4 \text{ s}^{-1}$. (C) Ultrafast uniaxial diffusion about the alignment axis ($D_{||} = \infty$) makes linewidths much narrower and essentially homogeneous.

In practice, however, the uniaxial diffusion rate depends on the size of the protein being studied. Figure 4 shows SLE simulations of a PISEMA experiment for a single helix in bicelles ($\theta = \pi/2$) at 20° orientation for a range of diffusion rates evaluated from

eq 27: $D_{||} = 8 \times 10^5 \text{ s}^{-1}$, $D_{||} = 2 \times 10^5 \text{ s}^{-1}$, and $D_{||} = 1 \times 10^5 \text{ s}^{-1}$. A 60 kHz B_1 field has been used, and a smoothing convolution with an intrinsic line shape having a 50 Hz width in the direct dimension and a 100 Hz width in the indirect (dipolar)

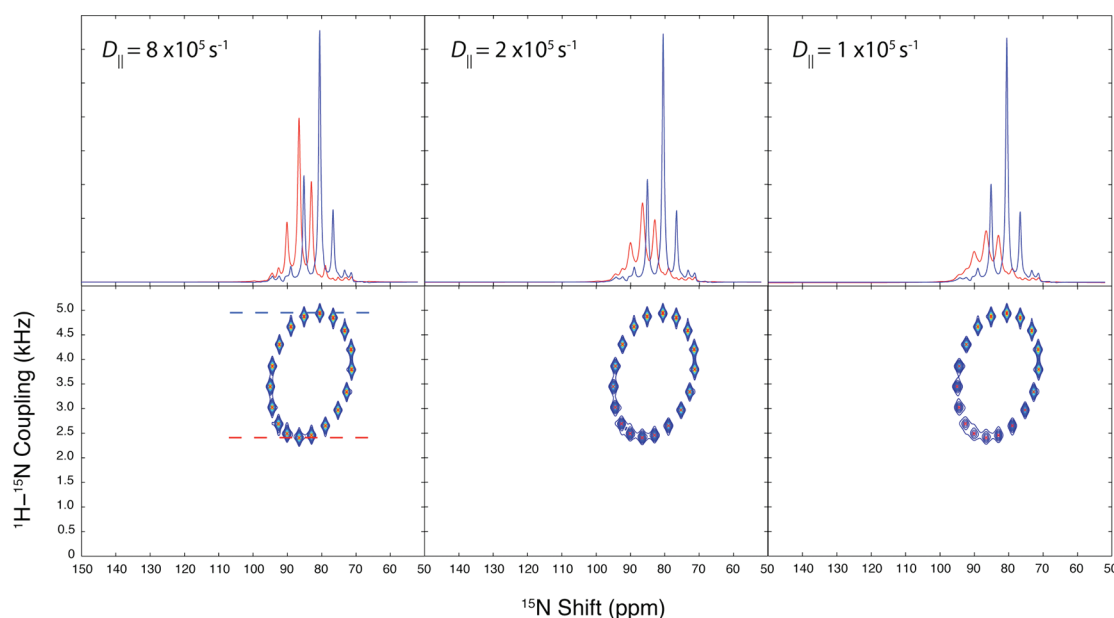


Figure 4. Effect of uniaxial diffusion on the motional narrowing of ^{15}N NMR resonance lines in magnetically aligned bicelles (perpendicular orientation). Calculations have been performed at various diffusion coefficients as shown. Slices through the dipolar dimension at the maximum (4940 Hz, blue lines) and minimum values (2405 Hz, red lines) for the dipolar couplings are shown in the top portion of the figure to illustrate the inhomogeneity of the line narrowing due to uniaxial diffusion.

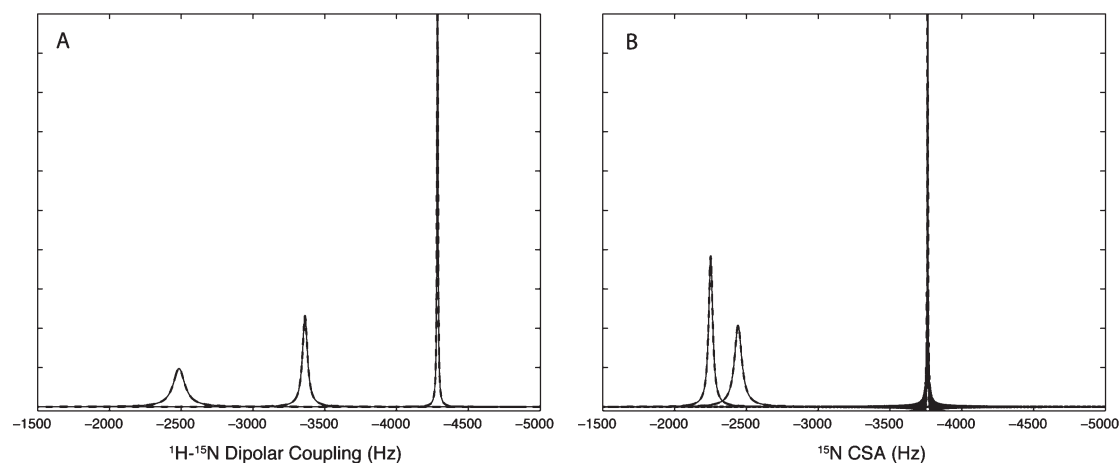


Figure 5. Comparison of the closed-form solutions (dashed lines) with the SLE simulations (solid lines) for the perpendicular bicelles assuming perfect decoupling for $D_{\parallel} = 10^5 \text{ s}^{-1}$. (A) Dipolar linewidths. (B) Chemical shift linewidths. Simulations have been performed for three representative residues of the α -helix, $n = 2, 3$, and 4 . The closed-form solution is essentially indistinguishable from that obtained from SLE at this motional rate.

dimension has been applied. Slices through the dipolar dimension at 2405 Hz (red) and 4940 Hz (blue) are shown on top of the two-dimensional spectra to illustrate the effect of inhomogeneous line broadening/narrowing for the largest and smallest dipolar couplings at the various values of D_{\parallel} . The linewidths are more homogeneous at the fastest diffusion rate considered, $D_{\parallel} = 8 \times 10^5 \text{ s}^{-1}$ (which would correspond to a single α -helical protein). At this rate, the dependence of the observable frequencies on the azimuthal angle φ (cf. eqs 1–3) is effectively averaged out by the motions. By contrast, a significant anisotropy in the observed linewidths is expected for larger membrane proteins having the uniaxial diffusion rate $D_{\parallel} = 1 \times 10^5 \text{ s}^{-1}$ and below (i.e., when the protein diameter exceeds 40 Å).

Comparison of the closed-form solutions, eqs 17 and 19, with the SLE solutions is given in Figure 5 and has been calculated for three representative residues within the helix, $n = 2, 3$, and 4 . For the SLE solutions, we have neglected the chemical shift effects during the evolution of the dipolar dimension and assumed perfect heteronuclear decoupling in the direct dimension. No filtering function has been applied. A diffusion coefficient of $D_{\parallel} = 10^5 \text{ s}^{-1}$ was used in the simulations; results for other diffusion coefficients are scalable linearly up to $D_{\parallel} = 10^4 \text{ s}^{-1}$. It has been found that the differences between the closed-form solution and SLE become more pronounced for the diffusion rates slower than 10^4 s^{-1} (results not shown). In those cases, the more rigorous SLE solution must be used. For faster diffusion rates, the

closed-form and SLE solutions are essentially indistinguishable (cf. Figure 5) and are represented by the Lorentzian shapes with the linewidths calculated from the relaxation rates given by eqs 17 and 19.

To further illustrate the inhomogeneity of the uniaxial narrowing in aligned samples, the calculated linewidths have been plotted in Figure 6 as a function of the residue number within the helix, yielding a rather complex periodic oscillatory function

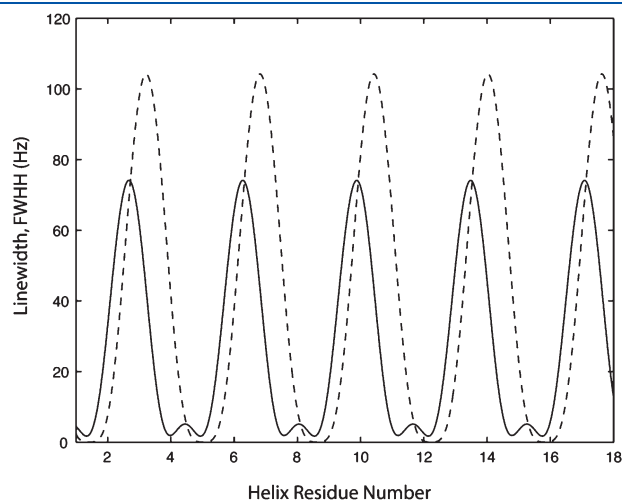


Figure 6. Variation of the ^{15}N CSA (solid lines) and ^1H – ^{15}N dipolar linewidths (dashed lines) within the helix at the 20° orientation calculated for the perpendicular bicelles at 750 MHz ^1H frequency and $D_{||} = 10^5 \text{ s}^{-1}$. The horizontal axis shows the index of the peptide plane within the helix. The linewidths due to global uniaxial diffusion are highly inhomogeneous within the helical structure.

reflecting the internal helical geometry. Note that the maximum narrowing in the dipolar dimension occurs when the orientation of the membrane normal relative to the molecular frame is close to $\beta_0 = \pi/2$, $\alpha_0 = \pi$, which may occur at a certain turn within the helical structure.

7. COMPARISON WITH THE EXPERIMENTAL DATA

The experiments have been performed on a Bruker Avance II NMR console operating at the ^1H frequency 500 MHz with a commercial E-free Bruker 5 mm round-coil probe. The uniformly ^{15}N -labeled Pf1 phage was purchased from Hyglos GmbH (Regensburg, Germany). The phage spectrum was acquired for 10 ms at the protein concentration ca. 45 mg/mL at -4°C , and a 6 s recycle delay, 64 scans, and 50.7 kHz B_1 rf field were used. To incorporate the Pf1 protein in bicelles, the sample was dissolved in 1 mL of TFE (50%)/TFA (0.1%), and the soluble protein fraction was lyophilized. About 5 mg of the lyophilized protein powder was reconstituted in DMPC/DHPC bicelles at a 3:1 molar ratio as described elsewhere.⁴⁰ For the bicelle-reconstituted protein, the sample temperature was maintained at 38°C , and a 20 ms acquisition time, 6 s recycle delay, 256 scans, and 40.3 kHz B_1 rf field were used. The data have been processed, and the linewidths have been determined using the NMRPipe software.⁴¹ No sine-bell apodization or linear prediction in the direct dimension was applied to any of the spectra.

Figure 7A shows the experimental PISEMA spectrum of the Pf1 phage acquired at 500 MHz. It should be noted that at 500 MHz and the given phage concentration the linewidths are slightly broader as compared to the previous studies⁴² performed at 750 MHz, most likely due to a weaker phage alignment. Therefore, the effect of static uniaxial disorder becomes more pronounced. Due to the overall phage length of about 20 000 Å,

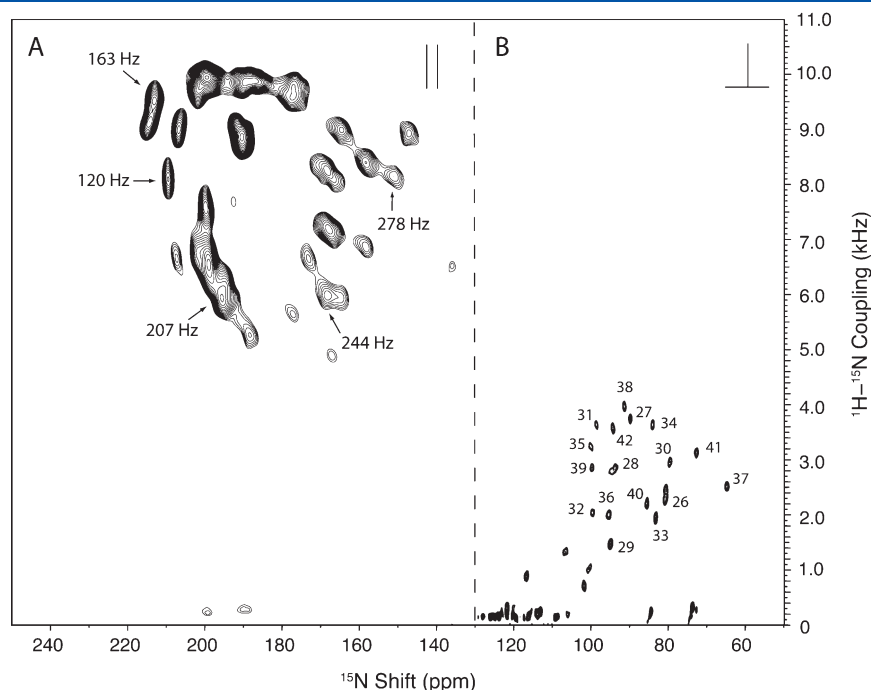


Figure 7. (A) PISEMA spectra of Pf1 expressed on a phage showing the predominant effect of uniaxial disorder. Various values for the linewidths within the spectrum are shown. (B) SAMPI4 spectra of Pf1 reconstituted in magnetically aligned bicelles. Spectroscopic assignments of the transmembrane helical portion of the protein from ref 45 are included. Static uniaxial disorder dominates the spectrum in part A, whereas fast uniaxial diffusion makes the lines much narrower in part B.

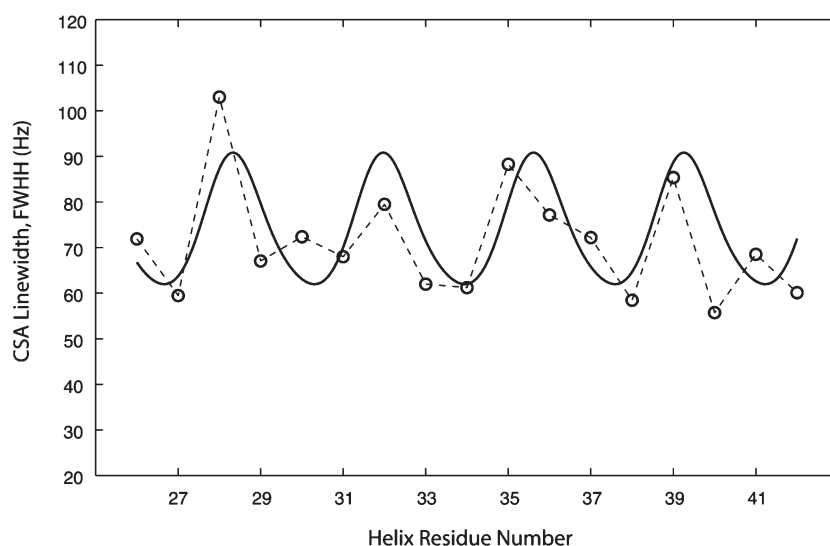


Figure 8. Fitting of the experimentally observed ^{15}N linewidths in the CSA dimension for residues I26-M42 of Pf1 reconstituted in magnetically aligned bicelles. The measured linewidths are given by circles connected by dash lines. The solid line shows the fit with $D_{\parallel} = 5 \times 10^5 \text{ s}^{-1}$, $\Delta\nu_{1/2}^{(0)} = 55.9 \text{ Hz}$, $\varepsilon = 0.47$, and 34.9° overall helix tilt relative to the bilayer normal. The ^{15}N CSA linewidths follow a general oscillatory behavior as expected for periodic helical structures.

uniaxial rotation is not possible, and the spectral linewidths are largely determined by the degree of alignment. Representative linewidths are given for select peaks, which show the linewidth distribution within the PISEMA ellipse similar to that expected for a static distribution.³⁹ A qualitative comparison with Figures 2 and 3 of the present paper and Figure 7 of ref 39 shows that the mosaic spread for this sample is between ± 1 and ± 2 degrees. By contrast, the SAMPI4 spectrum⁴³ for the perpendicular orientation of Pf1 in magnetically aligned bicelles (Figure 7 B) shows a much more narrow and uniform linewidth due to fast uniaxial rotation of the protein having the D_{\parallel} values on the order of 10^5 s^{-1} , as expected for single transmembrane helices. In this case, the total observed linewidths may result from a combination of fast uniaxial rotation, incomplete decoupling, and, possibly, local dynamics and heating of the sample due to rf irradiation.⁴⁴

Accurate experimental measurement of the spectral linewidths in oriented protein samples is in general difficult due to the relatively large number of scans needed and the requirement of high-temperature stability throughout the entire multidimensional experiment. In addition, some peaks may overlap, thus contributing to the error in measuring the individual linewidths. Moreover, the dipolar linewidths are largely affected by the performance of the decoupling pulse sequences, and accurate extraction of the dynamic information from this dimension would be even more challenging. Nonetheless, Figure 8 shows an attempt to fit the observed linewidths for residues I26-M42 of Pf1 in just the CSA dimension for the spectrum of Figure 7B using the closed-form solutions, eqs 17 and 19. The following semiempirical equation was used to fit the observed linewidths

$$\Delta\nu_{1/2}^{(\text{obs})} = \Delta\nu_{1/2}^{(0)} + \Delta\nu_{1/2}^{(\text{CSA})} + \varepsilon\Delta\nu_{1/2}^{(\text{DIP})} \quad (28)$$

Here the term $\Delta\nu_{1/2}^{(0)}$ describes the intrinsic line width, and ε is a parameter originating from incomplete heteronuclear dipolar decoupling. Uniform α -helical geometry was assumed, and the total of five fitting parameters was employed: the two Euler angles describing the tilt and rotation of the helix as a whole with respect to the bilayer normal (as contained in the angles $\alpha_0^{(1)}$ and

$\beta_0^{(1)}$ for the first observed residue), D_{\parallel} , $\Delta\nu_{1/2}^{(0)}$, and ε . Uniform chemical shift values were used for the fit, $\sigma_{11} = 64 \text{ ppm}$, $\sigma_{22} = 77 \text{ ppm}$, and $\sigma_{33} = 220 \text{ ppm}$. The previous assignment of Pf1 in magnetically aligned bicelles⁴⁵ was used. No linear prediction was used in either of the two dimensions, with the exception of a 30 Hz exponential multiplication to smooth out the noise. Taking into account the above-mentioned uncertainties, the fit of Figure 8 is quite good with an average deviation per residue of 6.9 Hz. The general oscillatory behavior of the linewidths characteristic of a helical structure is observed. An obvious outlier is the peak corresponding to G28, which strongly overlaps with G24, thus yielding an apparently larger line width. Variations in the chemical shift tensor values may also contribute to the deviations from the fit.

8. CONCLUSIONS

A general theory for two-dimensional solid-state NMR line shapes of oriented membrane proteins has been presented. Spin dynamics, structural geometry of the protein backbone, and global uniaxial disorder and rotational dynamics have been taken into account. A formulation based on the Stochastic Liouville Equation allows one to simulate the NMR spectra in both rigid and fast motional limits. Two-dimensional PISEMA spectra have been simulated by explicitly considering rf irradiation and frequency offsets in the direct and indirect dimensions. Closed-form solutions have been derived, which yield identical solutions to the SLE when the diffusion rates are sufficiently fast ($D_{\parallel} > 10^4 \text{ s}^{-1}$). The spectra were simulated for the cases of uniaxial disorder and diffusion of the helix as a whole, which affects inhomogeneously the lineshapes for the individual amide sites. Both dynamic and orientational effects can have a profound influence on solid-state NMR spectra of uniaxially aligned samples. Even a relatively small ($\pm 2^\circ$) mosaic spread can greatly broaden the NMR lineshapes; however, fast uniaxial diffusion can make this effect less pronounced. A detailed line shape analysis may allow one to extract information regarding the degree of mosaic spread as well as the motional rates. However, to extract

this information from the experimental data, one needs to quantify more accurately for the observed total linewidths, which should be addressed in the future studies. This, in turn, may allow one to use the linewidths as a complementary orientational constraint in addition to the widely used CSA and dipolar couplings. Uniaxial diffusion provides the predominant line narrowing mechanism in perpendicularly aligned bicelles, which makes them suitable for the structural and dynamical studies of membrane proteins having up to 40 Å in diameter. The presented formalism is generally applicable for calculating lineshapes for other NMR experiments in the presence of partial ordering and uniaxial rotations.

ACKNOWLEDGMENT

Supported by the National Science Foundation (MCB 0843520). The author wishes to thank Wenxing Tang for help with the preparation of the NMR samples.

REFERENCES

- (1) Howard, K. P.; Opella, S. J. *J. Magn. Reson. B* **1996**, *112*, 91–94.
- (2) Glover, K. J.; Whiles, J. A.; Wu, G.; Yu, N.-J.; Deems, R.; Struppe, J. O.; Stark, R. E.; Komives, E. A.; Vold, R. R. *Biophys. J.* **2001**, *81*, 2163–2171.
- (3) De Angelis, A. A.; Nevzorov, A. A.; Park, S. H.; Howell, S. C.; Mrse, A. A.; Opella, S. J. *J. Am. Chem. Soc.* **2004**, *126*, 15340–15341.
- (4) De Angelis, A. A.; Howell, S. C.; Nevzorov, A. A.; Opella, S. J. *J. Am. Chem. Soc.* **2006**, *128*, 12256–12267.
- (5) Park, S. H.; De Angelis, A. A.; Nevzorov, A. A.; Wu, C. H.; Opella, S. J. *Biophys. J.* **2006**, *91*, 3032–3042.
- (6) Park, S. H.; Marassi, F. M.; Black, D.; Opella, S. J. *Biophys. J.* **2010**, *99*, 1465–1474.
- (7) Park, S. H.; Prytulla, S.; De Angelis, A. A.; Brown, J. M.; Kiefer, H.; Opella, S. J. *J. Am. Chem. Soc.* **2006**, *128*, 7402–7403.
- (8) Prosser, R. S.; Hwang, J. S.; Vold, R. R. *Biophys. J.* **1998**, *74*, 2405–2418.
- (9) Park, S. H.; Loudet, C.; Marassi, F. M.; Dufourc, E. J.; Opella, S. J. *J. Magn. Reson.* **2008**, *193*, 133–138.
- (10) Park, S. H.; Das, B. B.; De Angelis, A. A.; Scrima, M.; Opella, S. J. *J. Phys. Chem. B* **2010**, *114*, 13995–14003.
- (11) Straus, S. K.; Scott, W. R. P.; Watts, A. J. *Biomol. NMR* **2003**, *26*, 283–295.
- (12) Esteban-Martin, S.; Strandberg, E.; Fuertes, G.; Ulrich, A. S.; Salgado, J. *Biophys. J.* **2009**, *96*, 3233–3241.
- (13) Holt, A.; Rougier, L.; Reat, V.; Jolibois, F.; Saurel, O.; Czaplicki, J.; Killian, J. A.; Milon, A. *Biophys. J.* **2010**, *98*, 1864–1872.
- (14) Nevzorov, A. A.; De Angelis, A. A.; Park, S. H.; Opella, S. J. In *NMR Spectroscopy of Biological Solids*; Ramamoorthy, A., Ed.; Marcel Dekker: New York, 2005; pp 177–190.
- (15) Park, S. H.; Mrse, A. A.; Nevzorov, A. A.; De Angelis, A. A.; Opella, S. J. *J. Magn. Reson.* **2006**, *178*, 162–165.
- (16) Spooner, P. J. R.; Friesen, R. H. E.; Knol, J.; Poolman, B.; Watts, A. *Biophys. J.* **2000**, *79*, 756–766.
- (17) Stein, R. A.; Hustedt, E. J.; Staros, J. V.; Beth, A. H. *Biochemistry* **2002**, *41*, 1957–1964.
- (18) Nesmelov, Y. E.; Karim, C. B.; Song, L.; Fajer, P. G.; Thomas, D. D. *Biophys. J.* **2007**, *93*, 2805–2812.
- (19) Cady, S. D.; Hong, M. J. *Biomol. NMR* **2009**, *45*, 185–196.
- (20) Abragam, A. *The Principles of Nuclear Magnetism*; Oxford University Press: London, 1961.
- (21) Redfield, A. G. *Adv. Magn. Reson.* **1965**, *1*, 1–32.
- (22) Traaseth, N. J.; Veglia, G. *Biochim. Biophys. Acta, Biomembr.* **2010**, *1798*, 77–81.
- (23) Gustavsson, M.; Traaseth, N. J.; Karim, C. B.; Lockamy, E. L.; Thomas, D. D.; Veglia, G. *J. Mol. Biol.* **2011**, *408*, 755–765.
- (24) Jo, S.; Im, W. *Biophys. J.* **2011**, *100*, 2913–2921.
- (25) Sharma, M.; Yi, M. G.; Dong, H.; Qin, H. J.; Peterson, E.; Busath, D. D.; Zhou, H. X.; Cross, T. A. *Science* **2010**, *330*, 509–512.
- (26) Wu, C. H.; Ramamoorthy, A.; Opella, S. J. *J. Magn. Reson. A* **1994**, *109*, 270–272.
- (27) Nevzorov, A. A.; Moltke, S.; Heyn, M. P.; Brown, M. F. *J. Am. Chem. Soc.* **1999**, *121*, 7636–7643.
- (28) Nevzorov, A. A.; Opella, S. J. *J. Magn. Reson.* **2003**, *160*, 33–39.
- (29) Engh, R. A.; Huber, R. *Acta Crystallogr., Sect. A* **1991**, *47*, 392–400.
- (30) Nevzorov, A. A. *J. Magn. Reson.* **2011**, *209*, 161–166.
- (31) Steeb, W. H. *Matrix Calculus and Kronecker Product with Applications and C++ Programs*; World Scientific: Singapore, 1997.
- (32) Kubo, R. *J. Phys. Soc. Jpn. Suppl.* **1969**, *26*, 1–5.
- (33) Freed, J. H. In *Electron spin relaxation in liquids*; Muus, L. T., Atkins, P. W., Eds.; Plenum Press: New York, 1972; pp 387–410.
- (34) Schneider, D. J.; Freed, J. H. *Adv. Chem. Phys.* **1989**, *73*, 387–527.
- (35) Bielecki, A.; Kolbert, A. C.; de Groot, H. J. M.; Griffin, R. G.; Levitt, M. H. *Adv. Magn. Reson.* **1990**, *14*, 111.
- (36) Saffman, P. G.; Delbruck, M. *Proc. Natl. Acad. Sci. U.S.A.* **1975**, *72*, 3111–3113.
- (37) Gurevich, V. V.; Gurevich, E. V. *Trends Pharmacol. Sci.* **2008**, *29*, 234–240.
- (38) Gurevich, V. V.; Gurevich, E. V. *Trends Neurosci.* **2008**, *31*, 74–81.
- (39) Quine, J. R.; Achuthan, S.; Asbury, T.; Bertram, R.; Chapman, M. S.; Hu, J.; Cross, T. A. *J. Magn. Reson.* **2006**, *179*, 190–198.
- (40) De Angelis, A. A.; Opella, S. J. *Nat. Protoc.* **2007**, *2*, 2332–2338.
- (41) Delaglio, F.; Grzesiek, S.; Vuister, G. W.; Zhu, G.; Pfeifer, J.; Bax, A. *J. Biomol. NMR* **1995**, *6*, 277–293.
- (42) Thiriot, D. S.; Nevzorov, A. A.; Opella, S. J. *Protein Sci.* **2005**, *14*, 1064–1070.
- (43) Nevzorov, A. A.; Opella, S. J. *J. Magn. Reson.* **2007**, *185*, 59–70.
- (44) Park, S. H.; Opella, S. J. *J. Am. Chem. Soc.* **2010**, *132*, 12552–12553.
- (45) Opella, S. J.; Zeri, A. C.; Park, S. H. *Annu. Rev. Phys. Chem.* **2008**, *59*, 635–657.